Advanced Steel Construction – Vol. 21 No. 2 (2025) 174–181
DOI:10.18057/IJASC.2025.21.2.8

EXPERIMENTAL STUDY ON SHEAR PERFORMANCE OF TWO-STORY COMPOSITE COLD-FORMED THIN-WALL STEEL EXTERIOR WALL

Yun-Peng Chu, Hui Xia * and Ya-Xin Xiao

School of Civil Engineering and Architecture, Southwest University of Science and Technology, Mianyang 621010, China
** (Corresponding author: E-mail: 2511830340@qq.com)*

ABSTRACT

This study investigates the shear performance of composite cold-formed thin-wall steel walls, particularly in two-story configurations. 9 test groups with varying axial compression and anchor bolt types were examined. Results show that, compared to single-story walls, the two-story walls exhibit lower energy dissipation and ductility, with floor joints being the weak link under cyclic loading. Out-of-plane instability and buckling failure often occur at the floor joint, which is critical to maintaining wall strength. The inter-layer tension bar has little effect on enhancing shear capacity. As axial pressure increases, out-of-plane instability worsens, and simply improving the vertical compressive strength of the floor joint with anchor bolts is insufficient to mitigate this issue. However, double-nut anchor bolts significantly improve the wall's load-bearing capacity. Therefore, the use of anchor bolts at floor joints is recommended to enhance the shear capacity of multi-story structures.

ARTICLE HISTORY

Received: 10 September 2024
Revised: 24 December 2024
Accepted: 1 January 2025

KEYWORDS

Cold-formed thin-wall steel two-story wall;
Cyclic loading;
Experimental study;
Shear performance;
Failure mode

1. Introduction

The composite cold-formed thin-wall steel two-story exterior wall composed of upper and lower single walls connected by a floor joint, formed by joining the boundary track with the top and bottom tracks through self-drilling screws. This construction method, where components are fabricated in the factory and assembled on-site, follows the technical specifications for low-rise cold-formed thin-walled steel framing buildings (JGJ/T 421–2018) [1]. The composite wall, connected by self-drilling screws, is subjected to external loads, enabling quick and straightforward industrialization of building construction.

Extensive experimental studies and theoretical analyses have been conducted to evaluate the shear performance of single-layer configurations of these walls. These results have been applied in engineering practice [2], and shaking table tests have shown good seismic performance under frequent (7-degree) and rare (9-degree) earthquakes. However, these walls tend to experience minor damages, such as screw dislodgment and cracking under large earthquakes [3]. In multi-story buildings, horizontal seismic impacts increase with the number of floors, raising concerns about whether the practices outlined in the specification [1] can effectively resist these heightened seismic effects.

The force transfer at the floor joint is discontinuous due to the construction method. When the top of the wall experiences horizontal seismic action, bending moments and shear forces develop at each floor level [4]. Existing wall seismic tests [5] indicate that the strain on the interlayer steel tension band increases significantly, whereas the strain on the inner layer steel tension band increases to a lesser extent. This discrepancy highlights that the connection quality between the upper and lower walls is a critical factor influencing overall structural resistance. Therefore, the negative impact of discontinuous interlayers on shear capacity must be considered. Experimental studies [6-8] have shown that reducing keel spacing improves the shear capacity of the wall by 9–31%, depending on the wall structure. This increase in bearing capacity is attributed to the increased number of self-drilling screws due to reduced spacing. Gad [9] emphasized that stud spacing influences the failure load of the panel cladding wall, while increasing the keel section size and thickness improves shear capacity but reduces ductility and energy dissipation. Alabi et al. [10] evaluated the direct strength method of thin-walled steel members under the combined action of long axis compression and bending. Hu et al. [11] proposed an analysis model and calculation formula for the shear capacity of PFCFS composite walls. Zhang [12] proposed a formula for calculating the shear capacity of cold-formed thin-walled steel composite walls based on threaded connection failure.

Research on shear performance has mainly focused on intermediate walls, with little consideration given to exterior walls. The exterior wall differs due to the solid alignment of panels on the outer side and a permanently established boundary track at the floor joint, resulting in asymmetry along the wall's thickness direction. This structural difference leads to distinct failure modes and shear performance when compared to intermediate walls. Therefore, it is crucial to conduct experimental research to clarify the shear capacity and failure modes of the TCS wall, and further derive the stiffness theory for the external wall.

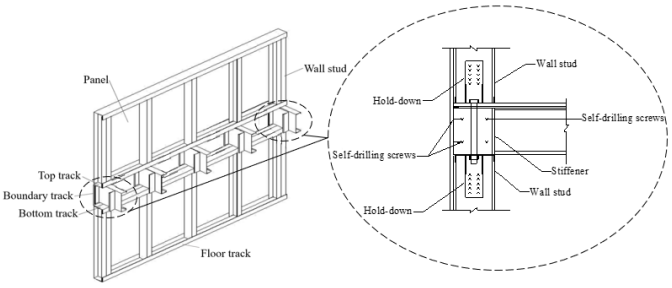

Fig. 1 Connection recommended by Regulation (JGJ/T 421–2018)

2. Experimental program

2.1. Material tests

The material utilized was Q235B galvanized steel with a nominal thickness of 1.0mm. The yield strength was improved due to multiple cold forming. Specimens followed the GB/T228.1–2010 [13] standard (Fig. 3). Three specimens underwent testing, yielding the following average results: a yield stress of 311.16 MPa, an elastic modulus of 160.19 GPa, and a yield strain of 0.19%. The fracture tensile strain reached 0.22, with the stress at fracture being 292.45 MPa. The ultimate strength recorded was 379.07 MPa, coupled with an elongation of 22.44%.

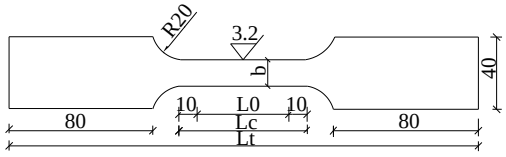

Fig. 2 Size of material properties specimen

2.2. Specimens design

9 specimens were designed based on different column web heights, types of anchor bolts and axial pressure ratios. The specimens were divided into 3 groups. The A group was the specimen with a web section height of 160 mm.

The B group was the specimen with a web section height of 89 mm. Through these two groups, the effects of different anchor bolt forms and different axial pressures on the shear performance of the wall were investigated. The C group was the specimen with a web section height of 89 mm basing on the specification [1]. It was used to obtain the influence of axial pressures on the shear performance of the wall.

All walls used double-sided cladding with full-scale sizes per specification [1]. Walls had 5 evenly spaced studs (3000 mm high) and 5 tracks (600 mm apart), with a 200 mm floor joint contributing to a total width of 2400 mm. Detailed component specifications are presented in Table 1. Wall studs were fixed to the boundary track with ST4.2 × 13 screws, spaced 100 mm apart (Fig. 3). The floor joint was 200 mm long. The wall stud at the boundary was an "I-shape" built-up section made of two C-sections (C89 or C160), while the central wall had a single C-section.

Table 1
Component specification

Components	Material	Specification
boundary track	thin-walled cold-formed steel	U200 mm × 40 mm × 1 mm
top and bottom tracks		U160 mm × 40 mm × 1 mm
floor track		C200 mm × 40 mm × 10 mm × 1 mm
wall stud		C160 mm × 40 mm × 10 mm × 1 mm
flat strap		40 mm × 1 mm

3 types of anchor bolts connected the wall sections: a-type, a 4.6-grade coarse bolt (40 mm diameter) with pressure-only nuts (Fig. 4(a)). The b-type anchor bolt (12 mm) was an anti-pull design with a nut and gasket at one end, relying on hold-down to transfer tensile pressure between floors and wall stud (Fig. 5(b)). The c-type anchor bolt (16 mm) had two pairs of nuts and gaskets at each end, forming a double nut design (Fig. 5(c)), allowing synchronized deformation of the top and bottom tracks. The differences in configuration was shown in Fig. 5. The specimen number and composition were shown in Table 2.

2.3. Test device

The testing apparatus primarily consisted of an MTS electro-hydraulic servo-controlled testing machine, a stationary frame, a reaction wall, a distribution beam, a ground track, and a reaction floor (Fig. 6). The distribution beam was constructed from 20a I-beam steel. During the experimentation, a 1000 kN jack was positioned atop the wall specimen. Between the distribution beam and the top track, a roller was placed, designed to move horizontally in tandem with the specimen, ensuring smooth load application. To mitigate specimen instability due to lateral eccentric loading, a support rod was horizontally positioned at the specimen's apex (Fig. 5). At the specimen's base, the U-shaped bottom track was bolted to the ground track using 20a channel steel, securing the assembly firmly in place. This setup was designed to maintain the integrity of the specimen under various loading conditions, allowing for accurate and reliable test results.

Table 2
Specimen number and composition

Serial number	Group	Specimens	Wall stud section (mm)	Vertical force (kN)	Number of anchor bolts	Panel type
1	A	WT-1	C160 × 40 × 10 × 1	30.2	2(b)	9mm Oriented strand board
2		WT-2	C160 × 40 × 10 × 1	40.3	2(b) and 3(a)	
3		WT-3	C160 × 40 × 10 × 1	30.2	2(b) and 3(a)	
4	B	WT-4	C89 × 44.5 × 12 × 1	40.3	2(b) and 3(a)	
5		WT-5	C89 × 44.5 × 12 × 1	30.2	2(b) and 1(a)	
6		WT-10	C89 × 44.5 × 12 × 1	40.3	2(b) and 3(c)	
7		WT-13	C89 × 44.5 × 12 × 1	30.2	2(b) and 3(c)	
8	C	WT-6	C89 × 44.5 × 12 × 1	40.3	2(b)	
9		WT-7	C89 × 40 × 10 × 1	30.2	2(b)	

Table 3
Test variables

Test variables	Specimens	Wall stud section (mm)	Vertical force (kN)	Number of anchor bolts
Wall stud section	WT-1	C160×40×10×1	30.2	2（b）
	WT-7	C89×40×10×1		
	WT-2	C160×40×10×1	40.3	2(b)+3(a)
	WT-4	C89×44.5×12×1		
Vertical force	WT-2	C160×40×10×1	40.3	2(b)+3(a)
	WT-3		30.2	
	WT-10	C89×44.5×12×1	40.3	2(b)+3(a)
	WT-13		30.2	
Number of anchor bolts	WT-1	C160×40×10×1	30.2	2（b）
	WT-3			2(b)+3(a)
	WT-4	C89×44.5×12×1	40.3	2(b)+3(a)
	WT-10			2(b)+3(c)
	WT-5	C89×44.5×12×1	30.2	2(b)+1(a)
	WT-12			2(b)+3(c)

2.4. Loading system

Prototype of the test was a 4-story cold-formed thin-walled steel house with a total height of 12 m. The length, width and each layer height were 12.8m, 10.8m and 3m respectively. The structural plane layout was shown in Fig. 7. The floor dead load, live load and the weight of the wall were 1.42 kN/m^2, 2.0 kN/m^2 and 1.0 kN/m^2 respectively. The weight of the doors and windows at the opening of the wall had been considered. The roof live load was 0.5 kN/m^2. Considering the conditions for 3-story and 4-story buildings, and referencing the calculation results in Section 4.4 of the monograph [14],

axial compressions of 30.2 kN and 40.3 kN were applied to the top of the wall during the experiment. The horizontal force was applied by a 1000 kN horizontal actuator.

The axial force on the specimen was applied in a single attempt, after which the initial displacement meter readings were documented. The loading system was detailed in Table 4. A low cyclic load was administered in the horizontal direction via displacement control, with increments of 5 mm per level. Each displacement stage was repeated thrice until the specimen succumbed to destruction.

2.5. Point arrangement

Strain data was captured using the DH3815N system, with ten strain gauges adhesively affixed to each specimen. The positioning of the strain gauges was illustrated in Fig. 8. Strain gauges numbered 1 through 5 were designated for assessing strain on the bolts, whereas gauges 6, 8, and 10 were tasked with gauging strain on the wall studs. Gauges 7 and 9 were specifically utilized for measuring strain on the diagonal tie bars. Fifteen YHD100 displacement meters were used: D1 for bottom track horizontal displacement, D2-D8 and D11 for wall elevations, D9-D10 for out-of-plane displacement, D12-D13 for vertical displacement at the base, and D14-D15 for the bottom track vertical displacement. The displacement and load values at the loading point were recorded using the displacement and force sensors attached to the actuator.

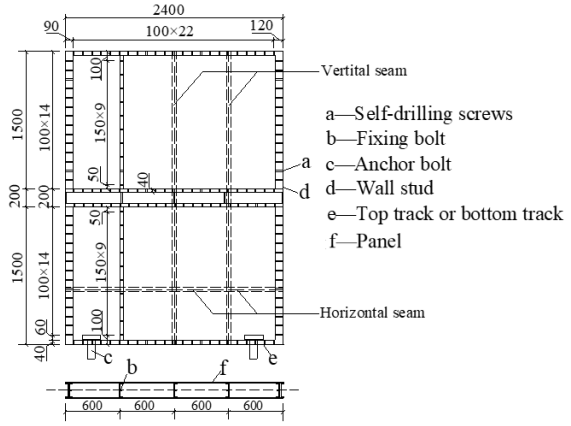

Fig. 3 The composite cold-formed thin-wall steel two-story exterior wall

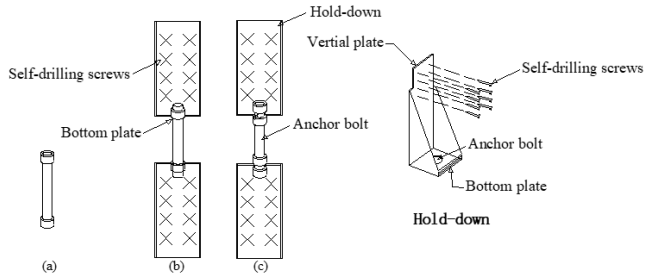

Fig. 4 Connection diagram

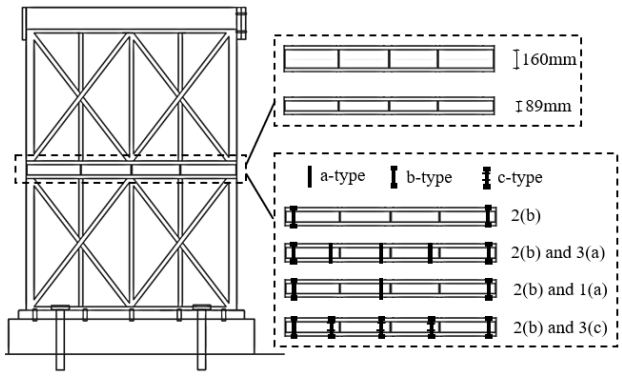

Fig. 5 Differences in configuration

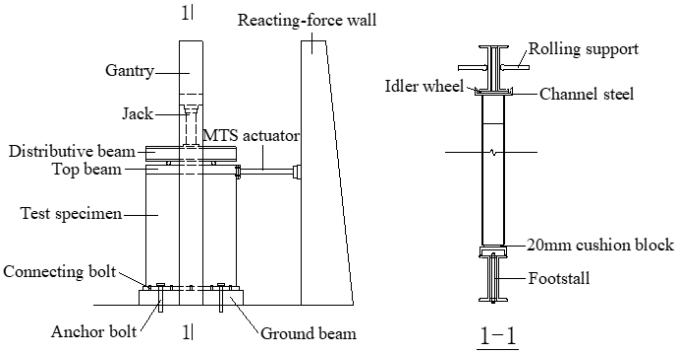

Fig. 6 Test equipment and site layout

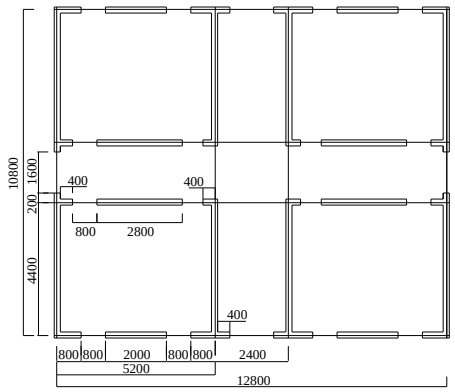

Fig. 7 Plan layout of the prototype

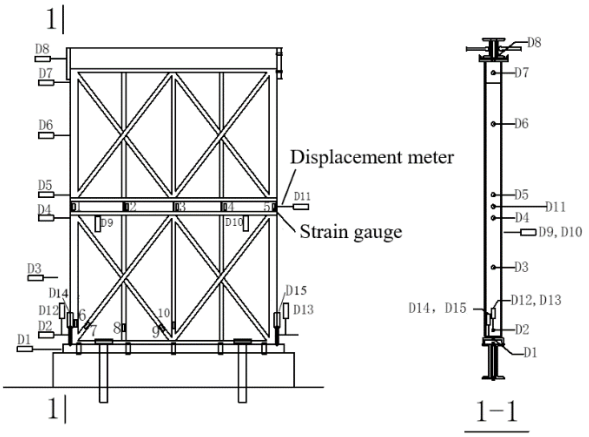

Fig. 8 Displacement meter and strain gauge arrangement

Table 4
Loading system

Load level	Displacement amplitude (mm)	Cycle index	Load level	Displacement amplitude (mm)	Cycle index
1	±5.0	3	2	±10	3
3	±15	3	4	±20	3
5	±25	3	6	±30	3
7	±35	3	8	±50	3
9	±55	3	10	±60	3
11	±65	3	12	±70	3

3. Test phenomena and failure characteristics

From the beginning of the test to the final destruction, it was divided into the following stages. Firstly, after the axial compression force was applied, the wall had a small out-of-plane displacement. Secondly, due to the discontinuity of the floor joint, the vertical load was transmitted to the floor track, the supporting stiffeners, and the boundary tracks, resulting in the local buckling

of the specimen. Finally, the self-drilling screws between the components were pulled out.

3.1. Group A

WT-1, designed per specification [1], showed small out-of-plane displacement at the floor joint after applying 30.2 kN vertical load (Fig. 9(a)). The out-of-plane displacement of WT-2 and WT-3 with three a-type anchor bolts was very small. The compressive capacity was obviously improved. When loaded to the limit state, due to the lack of constraints between the anchor bolt and the top and bottom tracks, the pressure is easily redistributed to the floor track after the anchor bolts fails, causing obvious buckling deformation (Fig. 9(b)). After the self-drilling screw at the corner of the wall was pulled out, the wall was separated from the keel (Fig.9(c)). After removing the outer OSB (oriented strand board), in addition to the obvious plastic deformation of the boundary track and the floor track, the keel of the upper and lower wall sections was intact (Fig. 9(d)). There was no local buckling of the bottom track. However, there is a vertical gap between the webs of the spliced section connected by self-drilling screws. In practical engineering applications, the self-drilling screws connected the two limbs should be encrypted.

3.2. Group B

WT-4 and WT-5 exhibited similar behavior. After applying axial compression, WT-5's floor track buckled slightly with one a-type anchor bolt. The WT-4 floor track with 3 a-type anchor bolts had no buckling. At a horizontal displacement of ± 35 mm, WT-5's floor track displayed localized buckling (Fig. 10(a)). Concurrently, the self-drilling screws connecting the corner panel to the keel failed (Fig. 10(b)). Local buckling occurred in the U-shaped track at the bottom of the wall stud (Fig. 10(c)).

After the three a-type bolts of WT-10 and WT-13 were replaced by c-type bolts, the compressive capacity was significantly improved. Upon applying axial compression to the top of the wall, the floor track exhibited no signs of buckling. When the horizontal loaded reaches ± 55 mm, the boundary tracks bulged outward obviously. The self-drilling screws connecting the wallboard and the keel at the floor joint squeezed the hole wall repeatedly. Then the screw hole on the panel became larger, and the slipping occurred between the drilling screw and the keel. The screw was pulled out when the loading displacement was greater. At the bottom, the self-drilling screws connecting the wall stud and the hold-down were damaged by shearing.

3.3. Group C

According to the practice of floor joint recommended by the specification [1], WT-6 and WT-7 showed similar failure modes. Upon the application of a horizontal displacement of ± 45 mm, pronounced local buckling was observed at the terminus of the floor track (Fig. 11(a)). During the continuous loading process, the boundary tracks bulged outwards. The out-of-plane deformation of the floor joint was obvious (Fig. 11(b)). The keel at the bottom of the wall stud was separated from the wallboard due to the pull-out of the self-drilling screws (Fig. 11(c)). Therefore, the number of self-drilling screws in this area should be increased. Local buckling of the bottom tack occurred under pressure. Compared with other specimens with the same vertical force, the failure characteristics appeared earlier and more obvious.

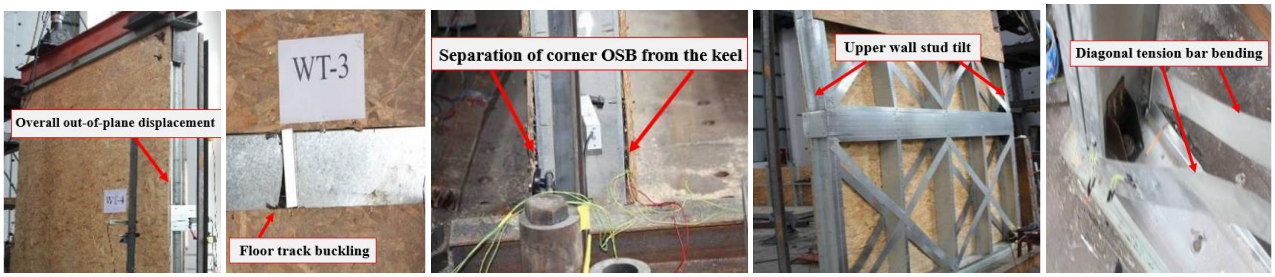

(a) (b) (c) (d) (e)

Fig. 9 Failure phenomena of A group. (a) Overall out-of-plane displacement. (b) Floor track buckling. (c) Separation of corner OSB from the keel. (d) Upper wall stud tilt. (e) Diagonal tension bar bending

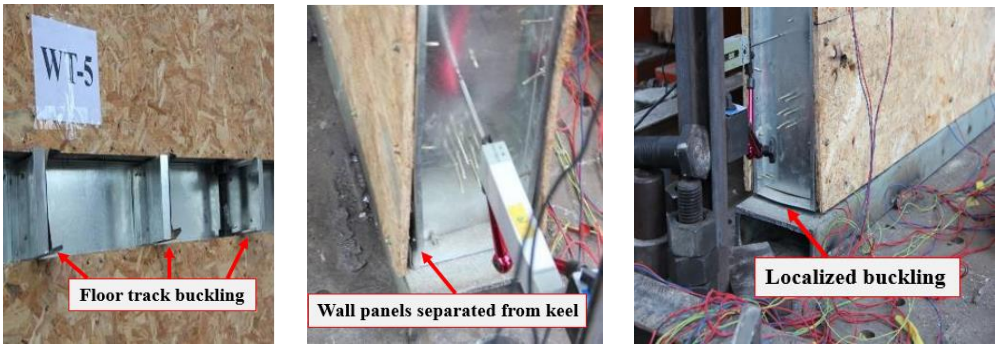

(a) (b) (c)

Fig. 10 Failure phenomena of B group. (a) Floor track buckling. (b) Wall panels separated from keel. (c) Localized buckling of the bottom track

(a) (b) (c)

Fig. 11 Failure phenomena of C group. (a) Boundary track buckling. (b) Wall panels separated from keel. (c) Self-drilling screws failure

4. Experiment results and analyses

4.1. Hysteresis curve

Load P was collected by the force sensor in the MTS actuator. Displacement Δ was the horizontal displacement of the top of the wall (at the upper guide rail). The load-displacement (P-Δ) curves of each specimen were shown in Fig. 12. Axial compression significantly impacted the energy dissipation capabilities of the specimens. Compared to specimens with an axial compression of 30.2 kN, those with an axial compression of 40.3 kN (WT-2, WT-4, WT-6, and WT-10) exhibited noticeably lower bearing capacity and reduced hysteresis curve characteristics. During the loading process of WT-4, the area of hysteresis curve increases little and no-load slip occurs. The reason was that the a-type anchor bolt end was lack of constraints under the cyclic load, which makes it prone to tilt failure. Top and bottom tracks were prone to local buckling failure after the failure of the anchor bolt. When WT-3 was loaded to -70mm cycle, WT-5 was loaded to ±40mm, and WT-13 was loaded to -45mm, the bearing capacity suddenly decreased. The main reason was the sudden out-of-plane displacement at the floor joint. Although the specimens can continue to bear load, their out-of-plane displacement increases significantly with loading. WT-6 and WT-7 were designed in adherence to the specification, with WT-6 exhibiting superior energy dissipation capacity than WT-7, thereby demonstrating the profound influence of axial compression on such specimens. Upon progressing to the failure state, the energy dissipation capacity of WT-6 and WT-7 remained relatively stable per cycle. The main reason was that the rigid motion of the upper and lower wall sections occurred almost along the floor joint and only the shear deformation of boundary track and the cyclic inclination of anchor bolts occurred at the floor joint. All the specimens had no apparent load drop section except for WT-3 and WT-5. For the side wall (wall single side with the boundary track), due to the asymmetric arrangement of structural members, the specimen had out-of-plane instability upon reaching the failure stage. As a result, most of the specimens had no obvious bearing capacity decline section. The local buckling of the floor track under compression led to a gradual reduction in the specimen's load-bearing ability. It can continue to bear the load, but the self-drilling screws on the external panel of the connection were loose. Consequently, the structural design should be enhanced to increase the compressive capacity of the floor joint. Merely bolstering the support stiffeners was insufficient to satisfy the load-bearing requisites.

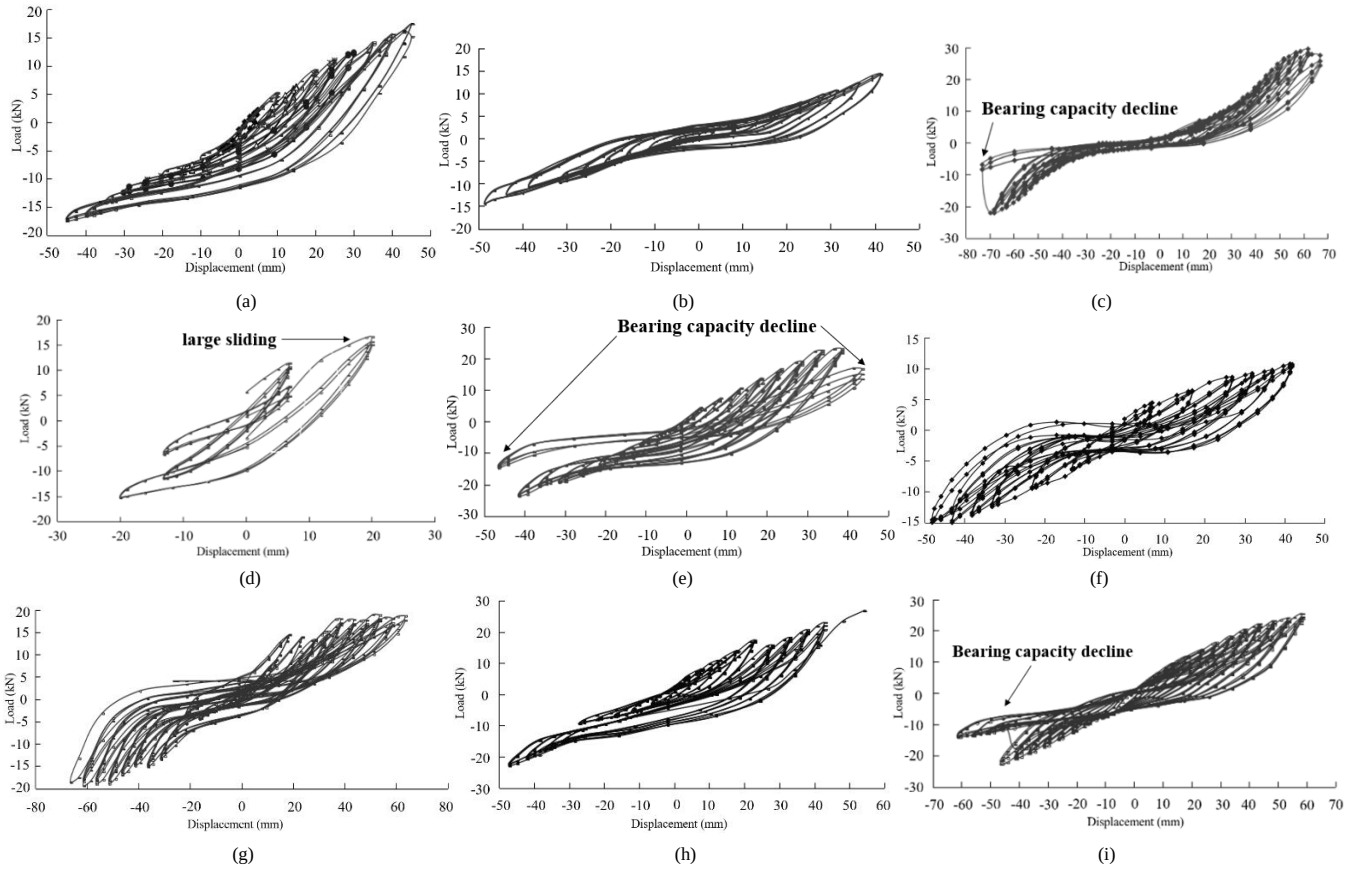

Fig. 12 Load-displacement curves. (a) WT-1. (b) WT-2. (c) WT-3. (d) WT-4. (e) WT-5. (f) WT-6(g) WT-7 (h) WT-10 (i) WT-13

4.2. Determination of yield point and failure load of specimen

The floor track exhibited significant deformation during loading, with the self-drilling screws at the edge of the floor joint becoming noticeably loose. According to European norms [15], 0.4 P_{max} was taken as the shear strength elastic limit of the wall, and that was the yield load. After loading to the ultimate load P_{max}, Sudden out-of-plane instability often occurred, resulting in the wall not continuing to load. Therefore, the failure load P_u took the same value as P_{max}. The P_y、Δ_y、P_{max}、Δ_{max}、P_u and Δ_u calculated by each specimen are summarized in table 5.

The bearing capacity of A group specimens was strongly influenced by both axial pressure and the type of anchor bolt used. With the same type of anchor bolts, the axial compression of WT-2 was higher than that of WT-3, resulting in a 51.8% reduction in ultimate bearing capacity. In contrast, WT-1, with three additional a-type anchor bolts, achieved at least a 26.8% increase in ultimate bearing capacity compared to WT-3. However, a comparison of WT-1 and WT-2 indicates that simply increasing the number of a-type anchor bolts did not significantly improve the bearing capacity. In Group B, following an increase in axial compression, WT-6 exhibited a 56.5% reduction in bearing capacity compared to WT-7. Additionally, the axial pressure had a considerable impact on specimens with extra anchor bolts, with WT-10 showing a minimum increase of 25.04% over WT-13. The C group further explored the effect of increased axial compression on bearing capacity. With increased axial pressure, the bearing capacity of WT-6 dropped by 56.5% compared to WT-7. On the basis of the C group of specimens, the B group was compared, which considered the increase of bearing capacity after adding different numbers of a-type anchor bolt. WT-5's bearing capacity was 1.22 times greater than that of WT-7, and WT-4's bearing capacity was 1.22 times higher than WT-6's. For the same count of different types of anchor bolts, WT-10's ultimate bearing capacity was 1.29 times that of WT-4, demonstrating a significant reinforcement effect. The inclusion of c-type anchor bolts markedly improved the shear capacity of the wall. However, the structural asymmetry caused by the boundary track and skin wall panels may lead to sudden out-of-plane instability, thus diminishing the wall's load-bearing capacity. Consequently, it is crucial to reinforce the out-of-plane support for the wall.

4.3. Energy dissipation and ductility performance

Cumulative energy dissipation is the sum of all hysteresis curve areas. The ductility coefficient is the ratio of the failure displacement to the yield displacement of the component ($\mu=\Delta_u/\Delta_y$). The cumulative energy dissipation and ductility coefficient were list in Table 5: When comparing identical structural specimens under varying axial compressions, it was found that WT-2's cumulative energy dissipation was 65.9% lower than that of WT-3, WT-6's was 67.7% lower than WT-7's, and WT-10's was 39.9% lower than WT-13's. As axial pressure increased, the cumulative energy dissipation capacity showed a clear decline. After adding 3 c-type anchor bolts, the influence of axial pressure was decreasing. The reason is that the double nuts reinforce the confinement of the top and bottom tracks. Consequently, the anchor bolts can more effectively synchronize the deformation between the upper and lower wall sections, thereby enhancing the resistance to failure. WT-10 exhibited an energy dissipation capacity that was 3.33 times higher than WT-4's, largely because WT-4 lacked the rod end restraint under cyclic loading. Following anchor bolt failure, the internal forces were redistributed to the boundary and floor track, exacerbating the specimen's out-of-plane instability. The ductility of the specimens was different after forward and reverse loading. Mainly because the forward loading was unstable and the reverse cannot continue to load. The anti-buckling ability of the floor track in the plane of the wall was improved after adding the c-type anchor bolt. Although minor deformations may lead to reduced energy dissipation capacity and ductility, there was a notable increase in the wall's bearing capacity.

Table 5
Summary of main test values

Specimens	Direction	Yield limit		Ultimate limit		Destructive load		μ	Ability to accumulate energy
		P_y(kN)	Δ_y(mm)	P_{max}(kN)	Δ_{max}(mm)	P_u(kN)	Δ_u(mm)		
WT-1	Positive	6.98	40.15	17.44	45.02	17.44	45.02	1.12	20952
	Negative	-6.98	-38.08	-17.44	-45.02	-17.44	-45.02	1.18	
WT-2	Positive	5.75*	17.31*	14.37	41.40	14.37	41.40	2.39*	10502
	Negative	-5.75	-20.40	-14.37	-48.63	-14.37	-48.63	2.38	
WT-3	Positive	11.91	34.71	29.77*	66.93	25.30	66.27	1.91	30768
	Negative	-8.85	-44.02	-22.12	-68.12*	-18.81	-70.50*	1.60	
WT-4	Positive	6.64	15.96	16.59	20.01*	16.59	20.01*	1.25	6263*
	Negative	-7.08	-25.75	-17.71	-26.21	-17.71	-26.21	1.02*	
WT-5	Positive	9.25	31.45	23.12	38.48	19.65	41.20	1.31	23929
	Negative	-9.51	-38.88	-23.77	-41.54	-20.20	-43.52	1.12	
WT-6	Positive	4.26	30.03	10.65	41.91	10.65*	41.91	1.40	8752
	Negative	-5.82	-36.70	-14.55*	-48.10	-14.55	-48.10	1.31	
WT-7	Positive	7.53	34.47	18.83	53.47	18.83	53.47	1.55	27080
	Negative	-7.76	-56.94*	-19.41	-61.57	-19.41	-61.57	1.08	
WT-10	Positive	9.17	33.16	22.93	42.81	22.93	42.81	1.29	20758
	Negative	-9.17	-26.20	-22.93	-47.23	-22.93	-47.23	1.80	
WT-13	Positive	10.16*	45.43	25.41	58.46	25.41*	58.46	1.29	34566*
	Negative	-9.10	-39.34	-22.75	-46.55	-19.33	-48.31	1.23	

Note: The parameter with * represents the maximum absolute value or the minimum absolute value of the parameter.

4.4. Rigidity degradation

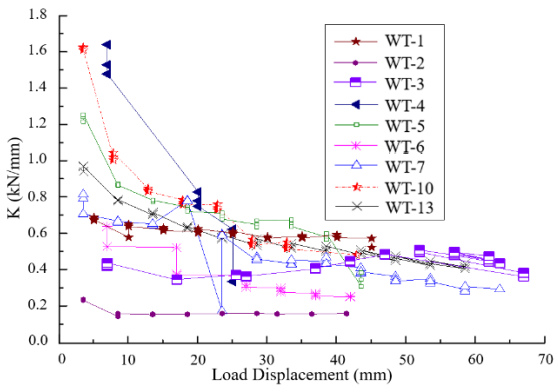

Fig. 13 Stiffness degenerated curve

The stiffness of the specimen under cyclic loading will decrease with the increase of the number of cycles and the load, which is called stiffness degradation. Rigidity can be expressed by ring stiffness *K*, referring to the method in regulation [16]. The stiffness degradation curve was shown in Fig. 13: The stiffness declined rapidly when the displacement reached between 10 mm and 30 mm. This rapid degradation was attributed to the detachment of self-drilling screws at this stage, coupled with local buckling of the floor track under compression. The accumulation of various damages caused the stiffness of the specimen to decrease. After the displacement was loaded to 60 mm, the specimen had out-of-plane displacement, resulting in the stiffness degradation to a minimum and unable to continue to bear. The degradation of WT-10 occurred more gradually compared to the other specimens, owing to the constraint imposed by the c-type anchor bolts on the top and bottom beams. Under cyclic loading, these bolts enabled better cooperation between the upper and lower wall sections, slowing stiffness degradation until the self-drilling screw disengaged. WT-4 had the maximum initial stiffness due to the increase of three a-type anchor bolts. But the degradation rate was faster. The reason was that the anchor bolt is fail, during the large displacement loading stage under cyclic load.

4.5. Strain-displacement curve

The strain-displacement curve was shown in Fig. 14. According to the material test, the yield strain was 1900×10^{-6}. The keel strain on all specimens had not reached the yield strain. When WT-10 was loaded to the failure state, the maximum strains of the middle vertical keel and the diagonal tension bar were 1826×10^{-6} and 121×10^{-6}, respectively, which proved that the material utilization rate was low and its effect was not obvious.

Under the same load, the keel strain of the A group of specimens was lower than that of the other groups. The maximum strain on the keel was 152×10^{-6} when loaded. The stress did not reach 10 % of the yield strength value. However, the self-drilling screw pull-out or out-of-plane instability of the whole wall had occurred, indicating that the material utilization rate was low after the cross section increases. In practice, reducing the keel section size may be considered.

The effectiveness of anchor bolts at the floor joint was pronounced. In WT-4, the anchor bolt's maximum micro-strain reached 1148×10^{-6} at the limit state. The maximum micro-strain of the WT-10 anchor bolt hit 1623×10^{-6}

upon failure. Therefore, incorporating c-type anchor bolts in engineering practice is recommended to improve the compressive strength of the floor joint.

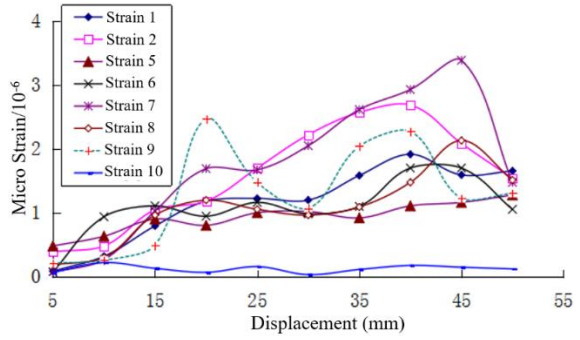

(a)

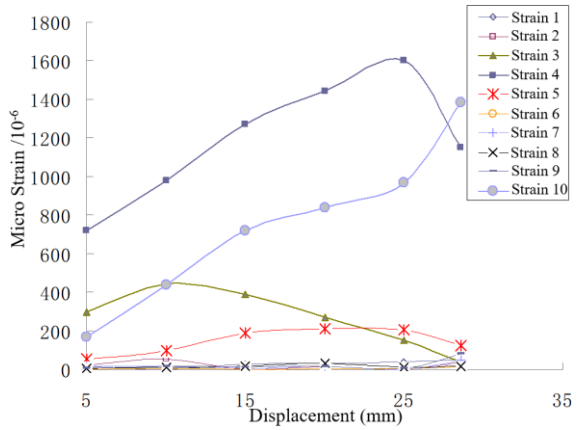

(b)

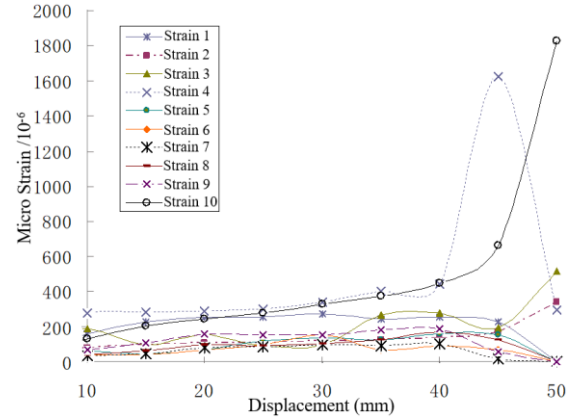

(c)

Fig. 14 Load-strain curve. (a) WT-1. (b) WT-4. (c) WT-10

5. Theoretical calculations of anti-lateral stiffness of the wall

The experimental data shows significant displacement at the floor joint, which requires attention. Given the current ambiguity in theoretical models, further refinement of stiffness calculations is necessary. This effort holds profound implications for structural assessment and offers valuable insights for the engineering design of the walls. At the initial stage of loading, the shear stiffness of anchor bolt is large. The lateral displacement at the floor joint is very small. The total lateral displacement of the wall is mainly caused by the lateral displacement of the upper and lower walls. But loaded to the late anchor bolt tilted. Following the tilting of the self-drilling screws on the shear member, the lateral stiffness becomes exclusively dependent on the boundary track and the external panels. Consequently, the lateral stiffness of the the wall's floor joint ought to encompass the lateral stiffness of the anchor bolt and the shear stiffness of the external panel. The shear stiffness calculation of the floor joint should include both the boundary track and the panel outside it.

5.1. Shear deformation calculation of wall panel

Fig. 15 is the shear deformation diagram of the boundary track and the external panel at the floor joint. It can be obtained Eq. (1) from $\tau = G\gamma$.

$$\frac{P}{Lt} = G\frac{\Delta_p}{H} \tag{1}$$

It can be seen from Eq. (1) that both the boundary track and the external panel of the floor joint can bear the shear force. It can be obtained Eq. (2).

$$\Delta_p = \frac{PH}{Lt_1G_B} + \frac{PH}{Lt_2G_S} \tag{2}$$

In which: Δ_p is the shear deformation of the wall panel. P is the horizontal shear force on the top of the wall. H is the height of the wall. L is the width of the wall. t_1 is the thickness of the external panel of the wall. t_2 is the thickness of the boundary track. G_B is the shear elastic modulus of the wall external panel. G_S is the shear elastic modulus of the boundary track. The shear deformation of the wall is shown in Fig. 15.

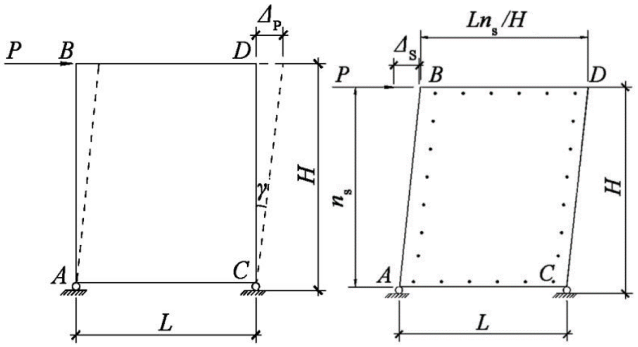

(a) (b)

Fig. 15 Shear deformation. (a) Shear deformation of wall panel. (b) Shear deformation caused by screws slip of wall panel

5.2. Shear deformation caused by sliding of self-drilling screws on wall panel

According to Reference [17], in the steel skeleton wall, the shear deformation caused by the slip of the self-drilling screw on the wall panel is calculated by the slip of the screw. Because the limit of panel size, a wall is often composed of many wall panels. There are joints between the two wall panels. The spacing between the surrounding and internal self-drilling screws of each wall panel is usually different. For the convenience of formula derivation, it is assumed: the actual wall is equivalent to only one wall panel. Screws are distributed around the panel, with uniform spacing in length and width directions, and the number is based on the average pitch. The shear force of each screw is equal and the screw slip is the same (Fig. 16). According to the above assumptions, the ratio of H to L is approximately equal to the ratio of the number of screws on the corresponding side. The shear force of a single screw is:

$$q_s = \frac{P}{n_s} * \frac{H}{L} \tag{3}$$

In which: P is the horizontal shear force on the top of the wall. n_s is the number of self-drilling screws along the height of the wall.

Under the action of P, the slip of a single self-drilling screw is S_s. According to the principle that the external force work is equal to the internal force work, it can be obtained Eq. (4).

$$P\Delta_S = 2q_sS_sn_s + 2q_sS_s \cdot \frac{Ln_s}{H} = 2PS_s\left(\frac{H}{L}+1\right) \tag{4}$$

That is:

$$\Delta_S = 2S_s\left(\frac{H}{L}+1\right) \tag{5}$$

fs is the shear force of the self-drilling screw to reach the maximum shear bearing capacity of the connection, and S0 is the slip at this time. Ss is the amount of screw slip when the maximum shear capacity is not reached. It can be obtained Eq. (6).

$$\frac{S_0}{S_s} = \frac{f_s}{q_s} \tag{6}$$

That is:

$$S_s = \frac{q_s S_0}{f_s} = \frac{PHS_0}{f_s n_s L} \tag{7}$$

Substituting the Eq. (3) and (6) into the Eq. (5), it can be obtained Eq. (8).

$$\Delta_S = \frac{2PHS_0}{f_s n_s L}\left(\frac{H}{L}+1\right) \tag{8}$$

5.3. Calculation of Horizontal Shear Deformation at Floor Joint

The calculation of horizontal shear deformation at floor joint includes the boundary track and the panel. The shear stiffness can be expressed as Eq. (9).

$$K = \frac{P}{\Delta} = \frac{Lt_1G_B}{H} + \frac{Lt_2G_S}{H} + \frac{f_s n_s L}{2HS_{01}\left(\frac{H}{L}+1\right)} + \frac{f_B n_s L}{2HS_{02}\left(\frac{H}{L}+1\right)} \tag{9}$$

That is:

$$\Delta = \frac{P}{K} \tag{10}$$

In which: H=2400 mm, L=200 mm, t_1=9 mm, G_B=1348.72 N/mm^2, t_2=1 mm, G_S=79230.77 N/mm^2, $f_b=\beta f_c dt_2$=1×205×4.2×1=861 N/mm^2, n_s=17, $f_s=f_B=\beta f_c dt$, f_c=25.83 N/mm^2.

Under the action of frequent earthquakes: S_{01}=0.35 mm, S_{02}=1.5 mm, substituted into the formula (10), it can be obtained $\Delta=1.28\times10^{-4}$P mm.

Under the action of rare earthquakes: S_{01}=1.25 mm, S_{02}=3.5 mm, substituted into the formula (10), it can be obtained $\Delta=1.30\times10^{-4}$P mm.

Through the calculation formula for the shear stiffness at the floor joint, the maximum lateral displacement can be further obtained. In the experiment, the bearing capacity of the wall is more than 10kN. Under the action of frequent and rare earthquakes, the maximum horizontal lateral displacement at the floor joint can be further obtained, which can reach 1.28mm and 1.3mm, respectively. Considering that the wall panel is relatively brittle, when loading to the elastic-plastic deformation stage under rare earthquakes, the OSB at the floor joint will be split due to shear action. To mitigate lateral displacement at the floor joint and prevent the failure of the outer panel following the tilting of anchor bolts, it is advisable to integrate reinforcing components at the floor joint.

6. Conclusion

The shear performance of the composite cold-formed thin-wall steel two-story exterior walls with different axial pressures and different types of anchor bolts is experimentally studied. The following conclusions are obtained:

(1) The self-drilling screws at the corner of the floor joint, the bottom of the wall, between the keels and between the keel and the wallboard are prone to loosening. Anti-pulling screws should be used to replace ordinary screws., and the number of self-drilling screws in these parts should be increased.

(2) Axial compression has a great influence on the bearing capacity and energy dissipation capacity of the wall. As the axial compression intensifies, the floor track becomes susceptible to local buckling and out-of-plane displacement at the floor joint, leading to a swift onset of instability and subsequent failure of the wall.

(3) The floor joint is the weak part of the wall. Utilizing the a-type anchor bolt enhances its compression resistance. However, due to the lack of rod end constraint, the cyclic load is easy to cause the failure of the anchor bolt. And then the pressure is redistributed to the floor track to cause rapid failure of the wall.

(4) Stress analysis reveals that the use of a double nut anchor bolt results in a 1.22-fold increase in load-bearing capacity. The bearing capacity is increased by 1.29 times and the energy dissipation capacity is increased by 3.33 times after using three double nut anchor bolts. The shear performance of the wall is obviously improved. It is recommended to use double nut anchor bolts at floor joints of multi-story buildings to enhance both load-bearing capacity and energy dissipation.

References

[1] JGJ227-2011 Technical specification for low-rise cold-formed thin-walled steel framing buildings, S. Beijing: China Architecture & Building Press, 2011.

[2] J.H. YE, Z.Y. Zhou. Discussion on light steel construction and development, J. Journal of Harbin institute of technology. 48 (6) (2016) 1-9.

[3] X.M. Zhai, X.X. Zha, K. Wang, et al. Shake table tests of a full-scale two-story plate-type modular composite building with semi-rigid corner connections, J. Engineering Structures. 289 (2023) 116-325.

[4] Y. Shi, X.W. Ran, G. Xiong, et al. Numerical modeling on shear performance of braced cold-formed steel composite walls, J. Journal of Constructional Steel Research. 198 (2022) 107-579.

[5] W.H. Liu, L. Deng, W.J. Zhong, et al. Parametric study on the pull-out performance of screw connections in cold-formed thin-walled steel structures, J. Engineering Structures. 274 (2023) 115-007.

[6] Liusi Dai, Xianzhong Zhao, Kim J.R. Rasmussen, Cyclic performance of steel storage rack beam-to-upright bolted connections, J. Journal of Constructional Steel Research. 148 (2018) 28-48

[7] Lewandowski MJ, Gajewski M, Gizejowski M, Numerical analysis of influence of intermediate stiffeners setting on the stability behaviour of thin-walled steel tank shell, J. Thin-Walled Structures. 90 (2015) 119-127

[8] Xu L, Martínez J, Strength and stiffness determination of shear wall panels in cold-formed steel framing, J. Thin-Walled Structures. 44 (10) (2006) 1084-1095.

[9] Gad EF, Duffield CF, Hutchinson GL, Lateral Performance of Cold-formed Steel-framed Domestic Structures, J. Engineering Structures. 21(1) (1999) 83-95.

[10] Song Hu, Li Zhou, Yong Huang, Experimental investigation on the seismic performance of phosphogypsum-filled cold-formed thin-walled steel composite walls, J. Thin-Walled Structures. 186 (2023) 110664.

[11] Xiuhua Zhang, Enyuan Zhang, Yizhuo Zhang, Study on shear performance of cold-formed thin-walled steel walls sheathed by paper straw board, J. Engineering Structures. 245 (2021)112873.

[12] M.A. Alabi-Bello, Y.C. Wang, M. Su, An assessment of different direct strength methods for cold-formed thin-walled steel beam-columns under compression and major axis bending, J. Structures. 34 (2021) 4788-4802.

[13] GB/T 228.1-2010(GB/T 228.1-2010 Metallic materials-Tensile testing, S. Beijing: Standards Press of China, 2010.

[14] Y.P. Chu, Y. Yao, Y.J. Deng, et al. Multi-storey ultra-thin-walled cold-formed steel structure housing system, M. Science Press. 2021.

[15] R. WANG, Y. YAO, Y.P. CHU. Wind-induced Response Numerical Simulation of Multilayer Cold-formed and Thin-walled Steel Structure under Different Wind Angle, J. Building Science. 11 (2015) 103-108.

[16] ECCS-TW1.3. Recommended testing procedure for assessing the behavior of structural steel elements under cyclic loads, R. ECCS Pub, 1986.

[17] Bai JL, Ou JP. Seismic failure mode improvement of RC frame structure based on multiple lateral load patterns of pushover analyses, J. Science China Technological Sciences. 54(11) (2011) 2825-2833.